Research Article

Determination of thermoelastic material properties by differential heterodyne detection of impulsive stimulated thermal scattering

B. Verstraeten [a], J. Sermeus [a], R. Salenbien [a], J. Fivez [b,*], G. Shkerdin [c], C. Glorieux [a]

[a] Laboratory of Acoustics and Thermal Physics, Department of Physics and Astronomy, KU Leuven, Celestijnenlaan 200D, B-3001 Heverlee, Belgium
[b] KU Leuven, Campus Brussels, Warmoesberg 26, B-1000 Brussels, Belgium
[c] Institute of Radio Engineering and Electronics of the Russian Academy of Sciences, Vvedensky sq., 1, Fryazino, Moscow Region, Russia

ABSTRACT

The underlying working principle of detecting impulsive stimulated scattering signals in a differential configuration of heterodyne diffraction detection is unraveled by involving optical scattering theory. The feasibility of the method for the thermoelastic characterization of coating-substrate systems is demonstrated on the basis of simulated data containing typical levels of noise. Besides the classical analysis of the photoacoustic part of the signals, which involves fitting surface acoustic wave dispersion curves, the photothermal part of the signals is analyzed by introducing thermal wave dispersion curves to represent and interpret their grating wavelength dependence. The intrinsic possibilities and limitations of both inverse problems are quantified by making use of least and most squares analysis.

© 2015 The Authors. Published by Elsevier GmbH. This is an open access article under the CC BY-NC-ND license (http://creativecommons.org/licenses/by-nc-nd/4.0/).

1. Introduction

The elastic and thermal characterization of functional materials plays a crucial role in the development of technological applications, with intriguing metrological challenges when the structural dimensions become of nanometric scale. Photoacoustics can provide a way to assess the elastic [1,2], thermal [3,4], optical and electronic characteristics [5–8] of materials through the observation the dynamics of optically excited thermoelastic displacement fields. In nanosecond to picosecond laser ultrasonics [9], a pulsed laser beam is employed to launch acoustic waves in and along the surface of a sample in order to determine the elastic properties and thickness of thin films [10–12] and to characterize nanostructures [13]. Laser ultrasonics can also be used as a non-destructive evaluation technique to reveal internal inhomogeneities such as cracks [14] and delaminations [15].

The unique potential of the photoacoustic approach and the steep evolution in the performance of lasers has stimulated many research groups to develop advanced electro-optical schemes and data acquisition systems. As a result, an extensive toolbox for optical excitation and detection of the laser-induced thermoelastic response of materials is now available. For the generation, both broadband and narrowband excitation setups are commonly employed. In broadband laser ultrasonic excitation, a simple optical lens system is typically used to focus a pulsed laser beam into a narrow point or line on the surface of the sample [16–18]. The generated guided acoustic waves have a broadband character as a consequence of the short laser pulse duration, and of the wide wavenumber spectrum that goes along with the sharp spatial features of the focused laser beam. Analysis of the dispersion of the velocity of the guided acoustic waves in a given wavelength range allows to determine absolute elastic properties of material layers as thin as the shortest wavelength, and relative changes in elastic parameters and thickness down to subnanometer scale [19–22].

When the experimental goals require the generation of monochromatic or narrowband acoustic waves, a transient grating excitation scheme can be used [23–25]. In this case, a spatially periodic light pattern, created by the interference of two crossing coherent beams from a pulsed laser, produces a transient light intensity grating on the surface or in the bulk of the sample. Optical absorption of the light energy then results in a heating and thermal expansion grating. As a result of the impulsive dynamics of this photothermal effect, it goes along with photoacoustic excitation of two spatially periodic counter-propagating acoustic wave packets. Both the thermal expansion grating, which gradually decays due to thermal diffusion between the hot and cold regions of the grating, and the propagating acoustic wave gratings, result in dynamic density gratings that go along with a spatially periodic ripple on

* Corresponding author. Tel.: +32 22101241

the surface of the sample and with a photoelastically induced refractive index grating. The diffraction of a probe beam by this grating then reveals the thermoelastic response of the material at a particular wavenumber. Historically, this transient grating technique has been referred to as impulsive stimulated scattering (ISS) [26–29]. A comprehensive review of more general laser ultrasonic detection schemes can be found in [30], discussing the principles of popular detection schemes that are either based on physical beam deflection [31,32], or on the interference of two probe beams [33–35].

In 1998, Maznev et al. [36] showed how heterodyne detection (HD) could be achieved for the ISS experiment, by introducing an optical scheme in which two coherent probe beams are used and in which the non-diffracted part of the second probe beam is collinear with the diffracted part of the first probe beam. In this approach, by virtue of the optical interference with the strong probe beam, the intensity and optical phase variations of the diffracted probe beam are substantially amplified, allowing the detection of very small density changes.

This article reviews the main elements of a HDISS experiment, from measurement to interpretation, with the focus on how to get the most of it and what to expect. For that purpose, Section 2 presents a differential approach to the heterodyne measurement technique delivering a signal which is directly proportional to the response of the material under investigation, free of any background and its accompanying fluctuations. Section 3 then addresses the inversion of the HDISS signal to material parameters for bulk material, based on thermoelastic theory. It is shown how to circumvent the numerical problem associated with the presence of two very different time scales. In Section 4, extension is made to a coating-substrate configuration. In that case the presence of the coating evokes a wavenumber dependence of an effective value for the thermal diffusivity, as extracted from the decay rate of the photothermal part of the signal. The basic features of this thermal wave dispersion behavior are discussed and the inverse problem, i.e. the extraction of thermal and elastic parameters from the signal, is tackled. A thorough sensitivity and uncertainty assessment is performed, by making use of most squares analysis, both for the photoacoustic and photothermal part of the HDISS signal. Section 5 summarizes the conclusions. The thermoelastic theory underlying the generation of light grating induced displacements is briefly summarized in Appendix A.

2. Heterodyne detection of ISS signals in a differential configuration

In this section, it is shown how the thermal response of a material can be measured in an ISS measurement. A differential heterodyne setup is presented, which yields a signal that is directly proportional to the thermoelastic response of the material under investigation, guaranteeing the best possible signal-to-noise ratio.

2.1. From setup to grating

ISS methods utilize narrowband photothermal/photoacoustic grating excitation [27] as schematized in Fig. 1. This can be achieved by crossing two coherent pulsed laser beams, generating a spatially sinusoidal interference pattern on the surface of a sample. A part of the pulsed (10 ps) excitation laser light is absorbed, resulting in a transient sinusoidal heat source with the same wavenumber as the one of the light pattern [26]. The impulsive heating leads to sudden thermal expansion, which in turns launches two counter propagating acoustic waves with the same wavenumber.

The two coherently interfering beams can easily be generated from a single pump laser beam by using a square relief grating
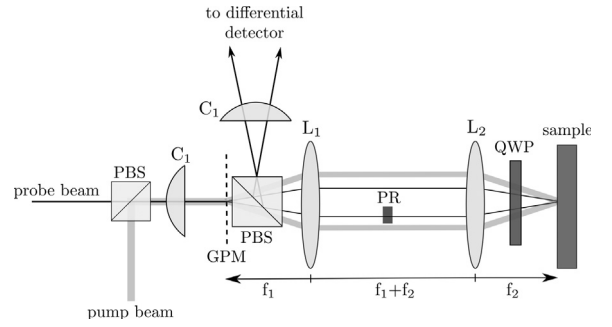
Fig. 1. Schematic overview of a differential heterodyne detection setup, with a polarizing beam splitter (BPS), a grating phase mask (GPM), a phase retarder (PR), a quarter wave plate (QWP), cylindrical lenses C_1 and spherical lenses $L_{1,2}$ with focal length $f_{1,2}$.

phase mask diffracting the light predominantly to the two first order directions. These two beams leave the phase mask at angles $\pm\theta$ with respect to the incident pump beam, given by

$$\sin\theta = \frac{\lambda_{pu}}{d}, \tag{1}$$

where λ_{pu} is the wavelength of the pump beam and d the phase mask spacing. The two beams can then be crossed on the sample surface with the aid of a two-lens imaging system (L_1L_2). When $d \gg \lambda_{pu}$, the angles of incidence $\pm\theta_{pu}$ are given by

$$\theta_{pu} = \frac{\lambda_{pu}}{Md}, \tag{2}$$

where $M \equiv f_2/f_1$ is the magnification of the optical system. The interference of the crossing beams at the surface of the sample then leads to an optical intensity pattern given by

$$I = I_{pu}(t)(1 + \cos(Kx)), \tag{3}$$

where the x-axis was chosen along the intersection of the sample surface and the plane defined by the crossing beams, with the origin $x = 0$ situated on the optical axis. $I_{pu}(t)$ represents the time dependence of the intensity of the pump beam pulse. The wavenumber K of the periodic light pattern at the sample surface is given by

$$K = 2k_{pu}\sin\theta_{pu} = \frac{4\pi}{\lambda_{pu}}\sin\theta_{pu} \approx \frac{4\pi}{Md}. \tag{4}$$

If there is no magnification ($M = 1$), then K equals twice the wave number of the phase mask.

The simultaneous presence of the two counter-propagating acoustic waves results in a standing wave pattern along the x-axis, leading to a beating normal displacement grating with wavenumber K, on top of the non-propagating thermal expansion grating, which slowly decays due to thermal diffusion. Choosing the y-axis perpendicular to the surface and restricting ourselves to the variable part of the displacement, the relief grating is then described by

$$y = h(x,t) = A(t)\cos(Kx). \tag{5}$$

The modulated ripple amplitude $A(t)$ represents the time dependence of the normal displacement due to the combination of thermal expansion and surface acoustic wave (SAW) motion.

2.2. From grating to heterodyne signal

2.2.1. Probing beams

In principle, the surface ripple induced by transient grating excitation can be locally detected by focusing a probe beam to a

spot that is much smaller than the grating spacing. In that case, the local displacement leads to measurable deflection and optical phase change of the probe beam, which can be detected respectively by a knife edge [37,30] or an interferometer [38–40] approach. The feasibility of such approach depends on the smallness of the focal probe beam spot, which is diffraction limited. In ISS, the probe beam spot is covering a region much larger than the grating wavelength, causing reflective diffraction into diffraction orders in addition to the specularly reflected beam, which represents the zero order diffraction component. In the experimental setup under consideration, a continuous probe beam with optical wavelength λ_p is superposed on the pump beam with the help of a polarizing beam splitter (PBS). Just like the pump beam, the probe beam is then split into two first order diffracted probe beams by the same grating phase mask that splits the pump beam. The two probe beams are then crossed again and, due to the periodic ripple, each of them is reflectively diffracted. A quarter wave plate (QWP) optimized for λ_p can be introduced to retrieve the reflected and diffracted probe beams at a second polarizing beam splitter right behind the grating phase mask, where they are guided towards a differential detector. The use of a cylindrical lens (C1) helps to focus the pump and probe laser light energy on a line in order to increase the thermal excitation and signal quality. As will be shown further, the differential heterodyne detection principle is based on phase quadrature between both incident probe beams, which is created by a phase retarder (PR) inserted in one of the beams.

2.2.2. Diffraction orders

The probe beams that are incident on the relief grating at the sample surface are reflectively diffracted into several orders. The diffraction efficiency for these diffraction beams will be shown to be a function of the angle of incidence of the respective probe beams, the ripple height, and the spatial period $D \equiv Md/2$. Fig. 2 schematically depicts one of the scattered beams for both probe beams. The electric fields of the incident probe beams can be expressed as

$$E_j = E_0 e^{i(\mathbf{k_j} \cdot \mathbf{r} - \omega t + \varphi_j)} \tag{6}$$

where ω is the angular frequency of the probe beams and $j = 1$, 2 refers to either of the incident beams. The wavevectors $\mathbf{k_j}$ are given by

$$\mathbf{k_1} = -k_p \sin\theta_p \mathbf{e_x} - k_p \cos\theta_p \mathbf{e_y}, \tag{7}$$

$$\mathbf{k_2} = k_p \sin\theta_p \mathbf{e_x} - k_p \cos\theta_p \mathbf{e_y}, \tag{8}$$
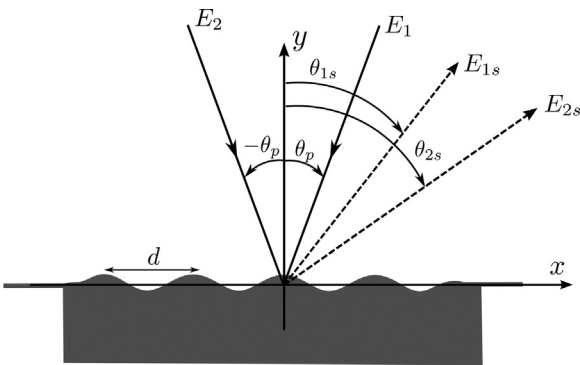
Fig. 2. Schematic presentation of the scattering process of the probe beams E_1 and E_2 incident at respective angles θ_p and $-\theta_p$. The electric fields E_{1s} and E_{2s} are diffracted fractions of probe beams E_1 and E_2 respectively, with diffraction angles θ_{1s} and θ_{2s}. Here the angles of scattering were chosen arbitrarily.

with $k_p = 2\pi/\lambda_p$. By symmetry, it can be assumed that both fields have an equal amplitude E_0. The optical phase difference $\Delta\varphi = \varphi_1 - \varphi_2$ between both beams can be controlled by the phase retarder.

In practice, the relief depth $h(x, t)$ caused by the pump beam is of the order of a few picometers to nanometers [41], which is much smaller than the relief period D varying from 1 μm to 100 μm. Therefore the scattered field can be expressed as a Rayleigh expansion [42], which is obtained by expanding the scattered field in a Fourier series along the grating direction x and by applying the Helmholtz equation [43] to obtain the wavenumbers in the perpendicular direction y. The diffracted field then reads as

$$E_{j,s} = \sum_{n_j=-\infty}^{+\infty} R_{n_j} e^{i\left(k_{n_j}x + \sqrt{k_p^2 - k_{n_j}^2}\, y - \omega t + \varphi_j\right)}, \tag{9}$$

where n_j denotes the order of the diffracted bundle originating from the jth incident probe beam, with a wave vector component along the x-direction given by

$$k_{n_j} = (2n_j + (-1)^j)k_p \sin\theta_p. \tag{10}$$

The amplitudes R_{n_j} represent the diffraction efficiency corresponding to the diffraction order n_j with scattering angle $\theta_{j,s}$. These angles are crucial as they determine which diffraction orders can be used to obtain the heterodyne interference. From Eqs. (9)–(10), the scattering angles for the different diffraction orders are found to be

$$\theta_{j,s}(n_j) = \tan^{-1}\left(\frac{(2n_j + (-1)^j)\sin\theta_p}{\sqrt{1 - (2n_j + (-1)^j)^2 \sin^2\theta_p}}\right). \tag{11}$$

In the following, we focus on the zeroth and first order diffracted beams. For the zeroth order ($n_j = 0$) diffracted beams Eq. (11) yields $\theta_{1,s}(0) = -\theta_p$ and $\theta_{2,s}(0) = +\theta_p$, corresponding to specular reflection off the surface. From here on, the zeroth order fields will be denoted respectively $E_{ref,1}$ and $E_{ref,2}$. For first order diffraction, Eq. (11) yields $\theta_{1,s}(1) = +\theta_p$ and $\theta_{2,s}(-1) = -\theta_p$, and we will denote the corresponding first order diffracted fields $E_{dif,1}$ and $E_{dif,2}$. It follows that the fields $E_{ref,2}$ and $E_{dif,1}$ are superposed in the direction θ_p. The superposed fields interfere, thus producing an intensity signal S_+ that can be captured with a detector. In the same way the fields $E_{ref,1}$ and $E_{dif,2}$ are superposed in the direction $-\theta_p$, resulting in the signal S_-. These signals, which are the basis of the heterodyne measuring technique, can be written as

$$S_+ = E_{ref,2} + E_{diff,1} = \left(R_0 e^{i\varphi_2} + R_+ e^{i\varphi_1}\right) e^{i\mathbf{k_+} \cdot \mathbf{r} - \omega t}, \tag{12}$$

$$S_- = E_{ref,1} + E_{diff,2} = \left(R_0 e^{i\varphi_1} + R_- e^{i\varphi_2}\right) e^{i\mathbf{k_-} \cdot \mathbf{r} - \omega t}, \tag{13}$$

where $R_+ \equiv R_{(n_1=+1)}, R_- \equiv R_{(n_2=-1)}$ and $\mathbf{k_+}$ and $\mathbf{k_-}$ are the signal beam wavenumbers given by

$$\mathbf{k_+} = k_p \sin\theta_p \mathbf{e_x} + k_p \cos\theta_p \mathbf{e_y}, \tag{14}$$

$$\mathbf{k_-} = -k_p \sin\theta_p \mathbf{e_x} + k_p \cos\theta_p \mathbf{e_y}. \tag{15}$$

It is important to note that the coincidence of both diffracted beams is a consequence of the underlying probes beams having been split by the same phase mask as the pump beams. Hence, guiding the probe beam through the same phase mask and optical path as the pump beam is a crucial aspect of this technique. In practice the probe and pump laser often have a different optical wavelength, so that the optical paths of the pump and probe

beams diffracted by the phase mask are not the same. Therefore, care should be taken to use lenses in the optical path with a minimum of spherical aberration. This is quite challenging for large diffraction angles, corresponding to short wavelength transient gratings.

2.2.3. Diffraction efficiencies

In order to calculate the heterodyne signals S_+ and S_-, expressions for the diffraction efficiencies R_0 and $R_\pm$ are needed. Here we assume a metallic surface, which is most interesting because it guarantees good reflection of the probe beam, but the results can be easily extended to dielectric surfaces [42]. For metallic surfaces, the diffraction efficiencies can be obtained by making use of the homogeneous Dirichlet boundary condition, which expresses that the sum of incident field (6) and diffracted field (9) is zero at the surface. Assuming that the expansion (9) for the diffracted field remains valid at the surface $y = h(x, t)$ [44], the homogeneous Dirichlet condition for the incident field E_j becomes

$$\sum_{n_j=-\infty}^{+\infty} R_{n_j} \left(e^{i\left(k_{n_j}x+\sqrt{k_p^2-k_{n_j}^2}h(x,t)\right)} \right) + E_0 e^{ik_p\left((-1)^j\sin\theta_p x - \cos\theta_p h(x,t)\right)}$$
$$= 0. \tag{16}$$

Multiplication by $\exp\left(-i\left(k_{m_j}x+\sqrt{k_p^2-k_{m_j}^2}h(x,t)\right)\right)/D$ and integration over one ripple then yields, using Eq. (7)–(8),

$$\sum_{n_j=-\infty}^{+\infty} R_{n_j} \left(\frac{1}{D}\int_{-D/2}^{D/2} e^{i\left((n_j-m_j)Kx+k_p\left(\sqrt{1-\left(\frac{k_{n_j}}{k_p}\right)^2}-\sqrt{1-\left(\frac{k_{m_j}}{k_p}\right)^2}\right)h(x,t)\right)} dx \right)$$
$$= -E_0 \left(\frac{1}{D}\int_{-D/2}^{D/2} e^{-i\left(m_j Kx+k_p\left(\cos\theta_p+\sqrt{1-\left(\frac{k_{m_j}}{k_p}\right)^2}\right)h(x,t)\right)} dx \right). \tag{17}$$

For low diffraction orders $k_{n_j,m_j} \ll k_p$, and the bracket on the left-hand side roughly equals δ_{n_j,m_j}. Hence, to a very good approximation the diffraction efficiency can be written as

$$R_{m_j} = -\frac{E_0}{D}\int_{-D/2}^{D/2} e^{-i\left(m_j Kx+k_p\left(\cos\theta_p+\sqrt{1-\left(2m_j+(-1)^j\right)^2\sin^2\theta_p}\right)h(x,t)\right)} dx, \tag{18}$$

where use was made of Eq. (10) and of the equality $K = 2k_p \sin\theta_p$, which was obtained from Eq. (4) by the observation that pump and probe beams pass through the same phase mask.

According to Eq. (5), at any particular moment the ripple generated by the pump beam is given by $h(x, t) = A(t)\cos(Kx)$. Using $DK = 2\pi$, the relevant diffraction efficiencies become

$$R_0 = -\frac{E_0}{2\pi}\int_{-\pi}^{\pi} e^{-i\xi\cos(x)} dx = -E_0 J_0(\xi), \tag{19}$$

$$R_+ = -\frac{E_0}{2\pi}\int_{-\pi}^{\pi} e^{-i(x+\xi\cos(x))} dx = iE_0 J_1(\xi), \tag{20}$$

$$R_- = -\frac{E_0}{2\pi}\int_{-\pi}^{\pi} e^{-i(-x+\xi\cos(x))} dx = iE_0 J_1(\xi), \tag{21}$$

where $\xi = 2A(t)k_p\cos\theta_p$ and J_n denotes the Bessel function of order n. As could have been expected from the symmetry of the relief grating, it turns out that $R_+ = R_-$.

2.2.4. Differential heterodyne ISS signal

Combining Eqs. (12)–(13) with Eqs. (19)–(21), the heterodyne signal intensities are found to be

$$I_+ = \frac{\epsilon_0 c}{2}|S_+|^2 = I_0\left(J_0^2(\xi)+J_1^2(\xi)+2J_0(\xi)J_1(\xi)\sin(\Delta\phi)\right), \tag{22}$$

$$I_- = \frac{\epsilon_0 c}{2}|S_-|^2 = I_0\left(J_0^2(\xi)+J_1^2(\xi)-2J_0(\xi)J_1(\xi)\sin(\Delta\phi)\right), \tag{23}$$

where $I_0 = \frac{\epsilon_0 c}{2}|E_0|^2$ is the intensity of the incident probe beam. Remark that I_+ and I_- are different in case of a phase shift between both probing beams, as obtained by the phase retarder in the setup.

The heterodyne signals consist of three parts. In practice, ξ is very small and therefore the first term, due to the zeroth order diffraction, is nearly constant. The second term, which would constitute the non-heterodyne signal obtained from the diffracted beam without the heterodyne superposition, is variable with varying relief depth, but is of second order and hence very small. Therefore the third term, which is due to the interference, constitutes the main dynamic part of the observed ISS signal. It is of first order and thus strongly amplified by the heterodyning effect. Nonetheless, the signals are still substantially dominated by the reference beam, whose noise and intensity fluctuations easily compete with the most important first order part of the signal. This affects the signal to noise ratio of the individual detector signals. This problem can be circumvented by electronically subtracting both heterodyne signals, which cancels the reference beam contribution and results in the differential heterodyne signal

$$S_{HD} = \frac{I_+-I_-}{2} = 2I_0 J_0(\xi)J_{+1}(\xi)\sin(\Delta\varphi). \tag{24}$$

When measuring S_{HD}, the sensitivity of the preamplifier after the differential photodiodes can be made very high without electronic overload caused by large reference beam contributions. The signal can be maximized by setting the phase retarder so as to create phase quadrature $\Delta\phi = \pi/2$ between the probing beams, which we will assume from now on. The background term S_{DC} is obtained by averaging both heterodyne signals as follows

$$S_{DC} = \frac{I_++I_-}{2} = I_0\left(J_0^2(\xi)+J_1^2(\xi)\right). \tag{25}$$

Because $\xi \ll 1$ the differential heterodyne signal can be rewritten to very good approximation as

$$S_{HD} = 2S_{DC}k_p\cos\theta_p A(t). \tag{26}$$

The signal depends linearly on the ripple modulation amplitude. Moreover, Eq. (26) allows direct retrieval of $A(t)$ without the knowledge of detector parameters.

The scalar treatment of the fields in the foregoing may suggest that Eq. (26) is only valid for an s-polarized probe beam, with its field in the z-direction. However, for p-polarization, separate versions of Eq. (16) can be written for the x-component and y-component of the fields, ultimately leading to the same result.

As an illustration, Fig. 3 shows the dependence of the two probe beam intensities on the ripple depth for $\lambda_p = 532$ nm and $D = 40$ μm. The linear relation between the differential heterodyne signal and the ripple depth is satisfied for modulation amplitudes exceeding 50 nm, and hence a fortiori for real experimental ripple magnitudes, which are typically less than 1 nm. For the non-differential heterodyne signals the ripple amplitude information is deeply buried in the signal.

2.3. Experimental aspects

In order to illustrate the typical outcome of a differential HDISS measurement, Fig. 4 depicts the fast transient thermoelastic decay
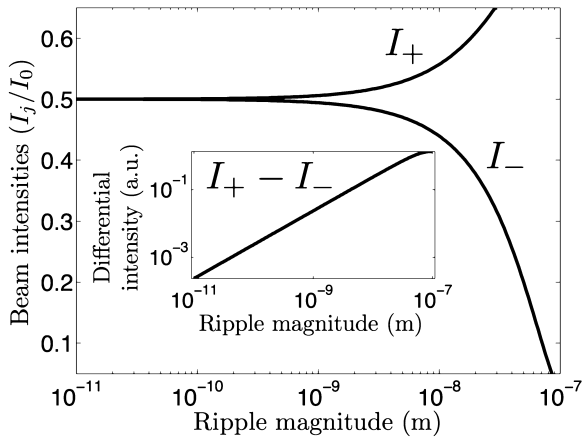
Fig. 3. Ratio of the signal beam intensities to the incident probe light intensity as a function of the ripple depth for a thermal grating spacing of 40 μm and a probe wavelength of 532 nm. The resulting difference signal is shown in the inset.
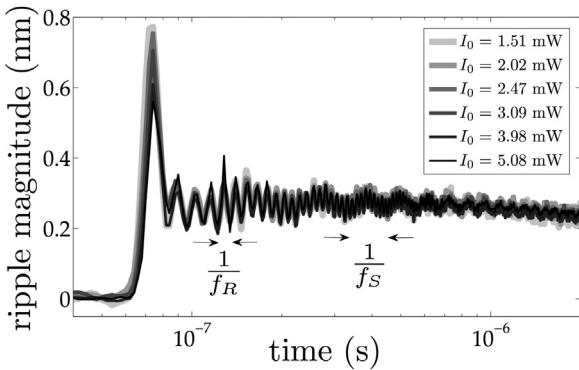
Fig. 4. Decay of the ripple magnitude of a 40 μm thermal grating on the surface of a glass substrate, as measured with six different probe beam intensities. The Rayleigh and Scholte frequencies are indicated. The peak value around t = 70 ns is caused by the presence of a thin aluminum coating. The noise floor of the signal is around 10 pm rms.

of the amplitude of a 40 μm thermal grating generated on a glass surface. In this experiment, thermoelastic signals were generated by a light pulse of 40 μJ from a Nd:YLF 1057 nm infrared pump laser Q-switched with a 1000 Hz pulse repetition frequency. The sample surface was coated with a 100 nm aluminum layer in order to increase the optical reflection. The probe light power generated with a 532 nm Nd:YAG CW laser was measured using a Thorlabs PM100D power meter. The heterodyne diffraction signal was detected by a fast AC coupled differential detector (Hamamatsu S5973 photodiodes with a Femto HSA (10 kHz–2 GHz) amplifier). The retrieved ripple magnitude did not vary much for probe beam intensities ranging from 1.5 to 5 mW, which illustrates the good signal-to-noise ratio of the differential technique.

The retrieved evolution of the ripple can be understood as follows. The impulsively generated thermoelastic stress is released by the generation of two counter-propagating Rayleigh SAW waves with frequency $f_R \approx 80$ MHz traveling along the surface with an amplitude in the order of 50 pm. The Rayleigh waves are accompanied by a slowly propagating interfacial Scholte wave [45] of frequency f_S = 8.5 MHz, for which no ripple amplitude can be extracted as it mainly modulates the phase of the probe beam via its effect on the local refractive index of the surrounding air. As the velocity of the Scholte wave is known to be very close to the speed of sound in air, the extracted frequency of the Scholte wave signature in the heterodyne signal can be used to check the value of the imposed wavelength.
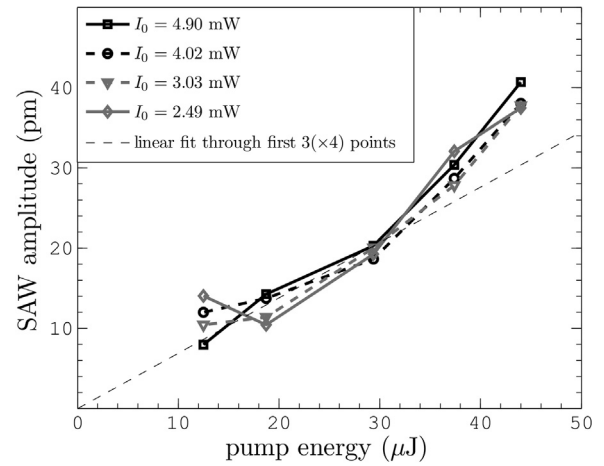
Fig. 5. SAW amplitudes extracted from the fast detector response as a function of the incident pump power, for four different probe intensities. The line through the origin represents a linear fit to the first 4 pump energy points for all probe intensities.

According to Fig. 4, the signal-to-noise-ratio of the full thermoelastic signal is good, but what really matters for the retrieval of the acoustic parameters is the signal-to-noise ratio of the SAW contribution, which inevitably is lower. In order to investigate this, thermoelastic signals were created for 5 different pump energies, and measured at four probe intensities. The SAW amplitudes were extracted after subtracting the Scholte wave and the slow-varying temperature decay from the signal. Fig. 5 shows the measured SAW amplitudes as a function of the incident pump energy. The difference between the measurements with different probe intensities shows that the signal-to-noise ratio is more than decent, except for the lowest pump energy. The nonlinear trend at higher pump energy is somehow unexpected and cannot be explained by a linear thermoelastic theory. It is probably related to the emergence of signal contributions due to ablation effects at high amplitudes.

When using Eq. (26) for the retrieval of the ripple amplitude, one should realize that the conditions leading to Eq. (26) are not fully achievable in practice. First of all, in the theoretical derivation, the thermal grating and probe beam are assumed to be extended to infinity along the x-direction. The finite size of the probe and/or pump beam affects the diffraction efficiencies, as the integrand in Eq. (18) should be convolved with the spatial profile of the laser beams. Secondly, roughness of the surface results in the addition of a spatially randomized component to the surface ripple modulation function in Eq. (5). In this case, the solution in terms of the Bessel function in Eq. (16) is altered, especially when the roughness domain scale is comparable with the probe beam width. Depending on the scale of the roughness, the diffraction angles are then modified randomly, breaking the symmetry of the excitation. Hence, the proposed laser ultrasonic excitation and detection technique is only fully suitable for optically reflecting samples with an adequate optical surface finish.

3. From HD signal to the physical material properties

In Section 2, it was shown how a HDISS experiment is able to produce a signal proportional to the magnitude of a thermally created surface ripple. The ultimate goal of the experiment is to retrieve thermal and acoustic material parameters. This section focuses on this inverse problem.

In an ISS experiment, the ripple amplitude modulation $A(t)$ originates from the response of the surface region of the sample to the incident pump power, through an intricate interaction of

thermal and elastic properties. An analytical inversion of $A(t)$ to retrieve the thermal and elastic material properties is therefore generally impossible. The way to go is to solve the forward problem for adequately chosen parameters in order to fit a representative simulated thermoelastic decay profile to the experimental one. For that purpose, a set of coupled differential equations must be solved. Appendix A briefly summarizes the thermoelastic theory underlying the generation of light grating induced displacements. In general, the integral in Eq. (A.21) can only be calculated numerically. However, some annotation can already be made based on the fact that, as expressed in the theorem of residues [46], the time dependence of the expression is determined by the singularities of the integrand in frequency domain.

It can be verified that there are three such divergencies. The first one is determined by $\sigma = 0$, governing the thermal decay process giving rise to a damped term. The other ones are the Rayleigh poles $\pm \omega_R$ [47], which are the only nontrivial zeros of the Rayleigh determinant D_R and give rise to an oscillatory term describing Rayleigh surface waves with the non-dispersive Rayleigh velocity $c_R = \omega_R/K$. As such, the ripple amplitude evolution is the superposition of a background with thermal decay time $\tau_{th} = 1/(K^2\alpha)$ and a smaller oscillatory part with the Rayleigh frequency ω_R.

The ISS technique is limited by the optical diffraction limit to grating wavelengths longer than 1 μm. As a consequence, in general, $\omega_R \gg 1/\tau_{th}$. Except for some temperatures and frequencies with strongly relaxing viscoelastic materials, the Rayleigh wave frequency is several of orders of magnitude larger than the thermal relaxation rate. In order to simulate a full thermoelastic decay process, i.e. well-sampled acoustics together with the thermal decay, the numerical Fourier integral should amply span the interval around both characteristic frequencies. For thermally fast materials (e.g. aluminum) and wavelengths smaller than 100 μm, this can be done by a standard desktop computer. However, for thermally slow materials the simulation of the thermoelastic decay can become problematic.

Another problem arises in the calculation of Eq. (A.21) at $\omega = 0$, where the Rayleigh determinant vanishes. This leads to a 0/0 situation, which is particularly delicate and leads to numerical instabilities at low frequencies. This is especially true for large wavenumber K, where D_R is the result of the subtraction of two large nearly equal numbers. This problem can, however, be circumvented by replacing, at low frequencies, the integrand by its series expansion to the lowest non-vanishing order [48]. As an example, Fig. 6 (top) shows (in arbitrary units) the integrand for

Fig. 6. Frequency dependence (top) and time dependence (bottom) of the ripple amplitude A (in arbitrary units) for the thermoelastic decay of a 40 μm thermal grating on the surface of a glass substrate. The dashed curve represents the low-frequency expansion. In the inverse Fourier transform yielding $A(t)$ the low-frequency approximation of $A(f)$ was used up to 10^6 Hz (vertical dashed line).

a 40 μm thermal grating on the surface of a glass sample. The glass parameters used in this simulation were $c_L = 5712$ m/s, $c_T = 3350$ m/s and $\alpha = 4 \times 10^{-7}$ m^2/s. For frequencies lower than 50 Hz, the numerical noise associated with the Rayleigh determinant becomes apparent. The low-frequency limit, which is close to the actual spectrum up to frequencies close to the Rayleigh pole ($f_R \approx 80$ MHz), is displayed in dashes. In order to simulate the full signal in time domain without numerical noise, a new combined frequency spectrum can be used that consists of the low-frequency limit at frequencies lower than a transition frequency f_c, and of the full expression at frequencies larger than f_c. Fig. 6 (bottom) shows the inverse Fourier transform of the combined signal of Fig. 6 (top) with $f_c = 1$ MHz $\ll f_R$. The non-zero value at the onset of the signal is a consequence of not taking into account frequencies above 5 GHz in the numerical integration.

The simulated ripple in Fig. 6 (bottom) contains four characteristics: the Rayleigh frequency, the thermal relaxation time, and the amplitudes of the thermal diffusion decay and Rayleigh wave contributions. In this way, apart from the Rayleigh velocity and the thermal diffusion, a best fit of a simulated profile to an experimental ripple can give access to two additional material parameters. Note that the damping of the simulated Rayleigh wave is related to the choice of the numerical finite value at the Rayleigh pole but has no further meaning. Experimentally, the width of the Rayleigh peak is determined by the acoustic damping of the SAW by the material and by the finite width of the beam.
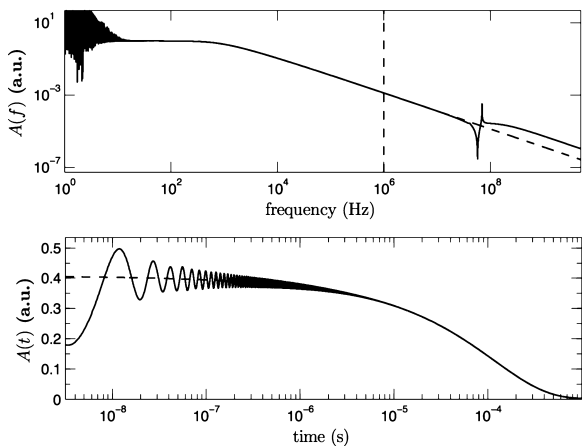
4. Differential heterodyne ISS for layered materials

Section 3 discussed the inversion of a HDISS signal for homogeneous materials. In this section, we discuss the feasibility of ISS together with heterodyne detection to characterize layered structures. Indeed, thin layered films are commonly used in modern industry, creating a need for fast and reliable non-destructive methods to gain knowledge of adhesion, thicknesses and various elastic properties. It is shown how the analysis of dispersion curves allows to retrieve material parameters, and how most squares analysis can be used to assess the uncertainty.

4.1. Dispersion curves

In layered structures, different geometrical and elastic parameters of each individual layer have an influence on the SAW propagation velocity, provided that the layer of interest is probed by the SAW. As was shown in Eqs. (A.10) and (A.11), the SAW displacement and stress fields decay exponentially with depth, with a characteristic penetration depth that is of the order of the acoustic wavelength. Therefore, SAWs with a wavelength that is very small compared to the thickness of the coating are unaffected by the substrate. Similarly, a coating much thinner than the wavelength will have no effect on the wave velocity, which will be the velocity for the substrate. However, when the thickness becomes comparable to the wavelength, the wave velocity is affected by the finite thickness of the coating. This gives rise to a wavelength dependence of the SAW, commonly depicted in a dispersion curve where the SAW phase velocity is plotted as a function of the wavelength or frequency of the wave. In addition to the Rayleigh type SAW dispersion, the perturbations traveling in the material can feel the existence of the interface between coating and surface, potentially giving rise to the excitation of surface waves at the interface, i.e. Stoneley and Sezawa waves [49].

For modeling a system with two layers, two sets of acoustical potentials and thermal fields are required. The coating is physically attached to the substrate and material from both sides of the interface is assumed to be in perfect adherence, without

introducing an elastic stress or a thermal resistance. Hence, the two sets of equations are coupled by boundary conditions expressing continuity of displacements and stress, temperature and heat flux. The solution of these equations gives rise to thermoelastic transients with acoustic frequency content and thermal diffusion rates depending on the thermal grating spacing and thermoelastic properties of the material. By using a similar approach as in Ref. [47], the acoustic dispersion curve of a fictive coating-substrate material ($c_{L,c}$ = 4000 m/s, $c_{L,s}$ = 7000 m/s, $c_{T,c}$ = 2000 m/s, $c_{T,s}$ = 4000 m/s, ρ_c = 8000 kg/m^3 and ρ_s = 3000 kg/m^3) with different coating thicknesses was calculated and is shown in Fig. 7. Although Rayleigh waves in many materials are intrinsically non-dispersive, the Rayleigh type mode shown in Fig. 7 (bottom) does depend on the frequency. Indeed, for large wavelengths compared to the coating thickness, or equivalently for low frequencies, the coating layer has no influence on the perturbations in the material and the Rayleigh velocity of the substrate ($c_{R,s}$ = 3683 m/s) is retrieved. As the applied frequency increases, the wavelength decreases until it becomes comparable to the coating thickness. Hence, the waves in this frequency range are affected by both layers, resulting in a velocity intermediate between the Rayleigh velocities of coating and substrate. When the frequency is increased further, eventually the wavelength becomes much smaller than the coating thickness, the coating itself appears as a semi-infinite half space with the corresponding Rayleigh velocity of the coating ($c_{R,c}$ = 1865 m/s). The Sezawa mode shown in Fig. 7 (top) has the longitudinal velocity of the substrate layer as a low frequency limit and the transverse velocity of the coating as high frequency limit. Note that when the Sezawa dispersion curve crosses the longitudinal velocity of the coating or the transverse velocity of the substrate, a wiggle appears. Also remark that the thickness of the coating fully determines the location of the sigmoidal transition of the dispersion curves. As a matter of fact, both for Sezawa and Rayleigh waves, the dispersion curves for different coating thickness would reduce to a single one when plotted versus the product of frequency and coating thickness. However, we preferred to plot them versus frequency alone for the sake of visualizing which frequencies are needed in practice to characterize coatings of different thicknesses.
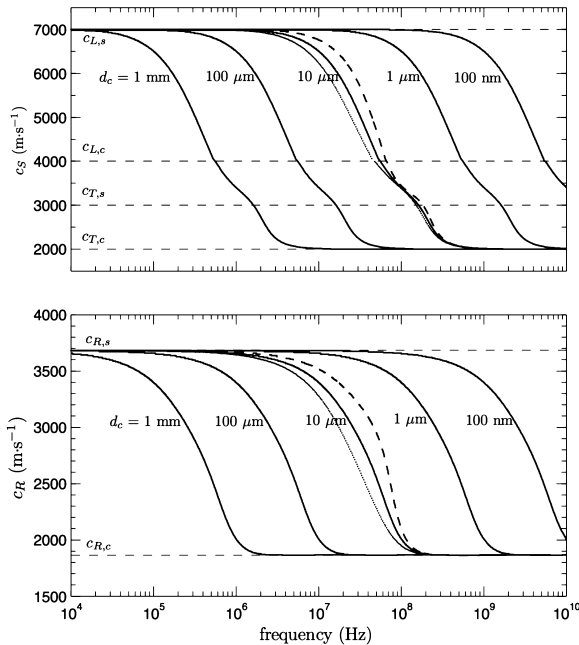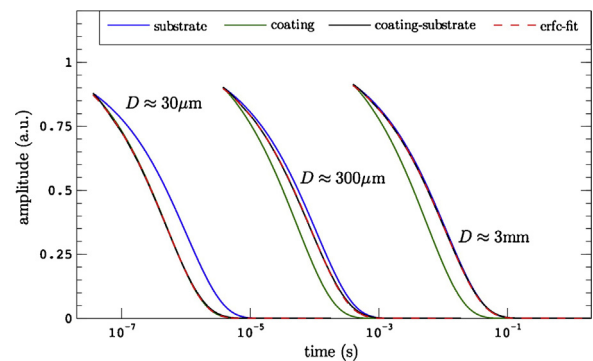
As solutions of the thermal diffusion equation constitute a thermal wave-like behavior, with a frequency dependent penetration depth (see Eq. A.6), one can envisage, in analogy with acoustic waves, thermal dispersion curves for multilayered materials, which express the observation that thermal diffusion rates change with frequency or imposed grating spacing. Käding et al. showed in [50] that the normal displacement at the surface ($y = 0$) of a semi-infinite substrate in the low-frequency limit of the thermoelastic equation follows a complementary error function evolution

$$u_y(y = 0) \propto \mathrm{erfc}(\sqrt{t/\tau_{th}}), \qquad (27)$$

where $\mathrm{erfc}(x) = 1 - \mathrm{erf}(x)$ is the complementary error function. The decay time $\tau = 1/(K^2\alpha)$ of this complementary error function, which sets the characteristic time scale for the thermal diffusion, corresponds with a thermal diffusion depth $L = 2\sqrt{\alpha\tau} = D/\pi$. For thermoelastic signal calculations for a gaussian excitation beam we refer to Baesso et al. [51], who modeled the photothermal displacements in a thermal mirror geometry, and to Todorovic et al. [52,53], who modeled thermoelastic bending in membranes.

In analogy with SAW, the thermal diffusion depth can be regarded as the depth to which the surface temperature field is sensitive to the thermal properties of the structure. Thus, for a given coating thickness d_c one expects that in the limiting case when $D \gg d_c$ the thermal decay process will be governed by the thermal properties of the substrate only. In the opposite limit $D \ll d_c$, the temperature field is concentrated in the coating and is hardly affected by the thermal properties of the substrate. Therefore, using different grating spacings, the depth-dependent thermal properties of the multilayer can be probed. For this, Käding et al. proposed to make use of an effective thermal diffusivity, which takes a value between the thermal diffusivities of the coating and substrate material for intermediate thermal diffusion depths $L \approx d_c$. The thermal decay in the multilayered structure is then fitted assuming a complementary error function to extract the effective diffusivity α_{eff}. In Fig. 8 the thermal decay in a fictive coating-substrate material ($\alpha_1 = 2 \cdot 10^{-5}$ m^2/s and $\alpha_2 = 1 \cdot 10^{-5}$ m^2/s) with a coating thickness of 1 mm is shown, together with the fitted erfc and the reference signals of pure coating and pure substrate material. Thermal wave dispersion is readily visible by observing the shift of the full coating-substrate signals from the reference pure coating to pure substrate signal with increasing grating spacing D. By estimating an effective diffusivity for various diffusion depths of the thermal wave field, a thermal dispersion curve can be constructed as shown in Fig. 9. In the limit of small diffusion depth, the effective diffusivity equals the coating diffusivity, as expected. For increasing diffusion depth, the

Fig. 7. Dispersion of the Sezawa mode velocity c_S and Rayleigh mode velocity c_R of a fictive coating-substrate material. For d_c = 10 μm the influence is shown of changing ϵ_ρ by +40% (dotted line) or −40% (dashed line).

Fig. 8. Amplitude of transient thermal gratings with three different spacings D in a fictive substrate material covered by a 1mm coating (black). For reference, the corresponding amplitudes are added for pure substrate material (blue) and pure coating material (green). The red line shows the best fitting complementary error function with an effective diffusivity.
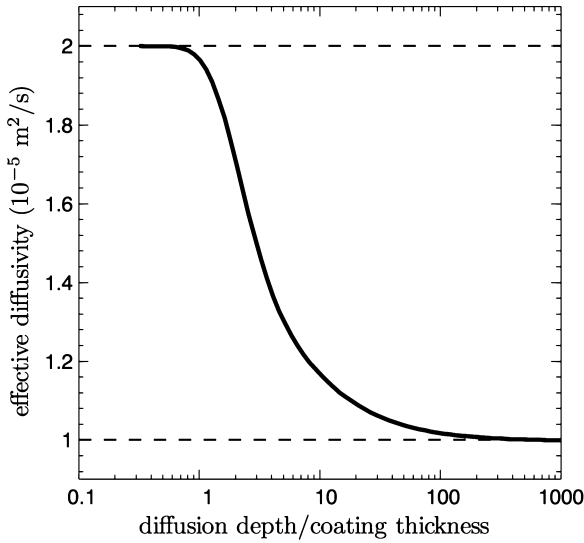
Fig. 9. Thermal wave dispersion curve depicting the effective thermal diffusivity of a fictive material consisting of a coating ($\alpha_1 = 2 \cdot 10^{-5}$ m²/s) on a substrate ($\alpha_2 = 1 \cdot 10^{-5}$ m²/s) as a function of the dimensionless ratio of the diffusion depth L to the coating thickness d_c.

effective diffusivity monotonically decreases and converges to the thermal diffusivity of the substrate layer.

### 4.2. Most-squares analysis of the inverse problem

An acoustic or thermal dispersion curve can be seen as the elastic or thermal fingerprint of a multilayered system. The experimental access to a dispersion curve provides a direct means to extract some of the elastic and thermal parameters by solving the inverse problem. In Ref. [11], it was shown that the inverse problem of extracting the elastic properties and thickness of a subsurface layer in a multilayer structure through ISS is well-posed, provided that both the Rayleigh and Sezawa modes are experimentally available. In experiments where only the Rayleigh mode is accessible due to non-ideal experimental conditions, the inverse problem is only feasible when no more than one coating layer is covering the substrate.

Four independent parameters can be retrieved from the Rayleigh dispersion. The Rayleigh velocities $c_{R,1}$ and $c_{R,2}$ of coating and substrate material can be obtained from the high and low frequency limits of the measured SAW dispersion curves. The position and shape of the transition is fully determined by the coating thickness d_c and the density ratio $\epsilon_\rho = \rho_1/\rho_2$ [54], which serve as third and fourth fitting parameter.

In general, the inverse problem is solved by minimizing a multiparameter χ^2 cost function to extract plausible system parameters. In order to illustrate the method and its pitfalls, we discuss the inverse extraction of the parameters ($\epsilon_\rho, c_{R,1}, c_{R,2}, d_c$) from the Rayleigh dispersion for a theoretical coating-substrate system with actual parameters ($\epsilon_\rho^* = 2, c_{R,1}^* = 3218$ m/s, $c_{R,2}^* = 5908$ m/s, $d_c^* = 10^{-5}$ m). In order to mimic real experimental data, white Gaussian noise with a standard deviation of 100 m/s was added to this dispersion curve, which is shown in Fig. 10. The χ^2 cost function for a trial set of parameters ($\epsilon_\rho, c_{R,1}, c_{R,2}, d_c$) was calculated according to

$$\chi^2(\epsilon_\rho, c_{R,1}, c_{R,2}, d_c) = \frac{1}{N} \sum_{i=1}^{N} (c_R(f_i, \epsilon_\rho, c_{R,1}, c_{R,2}, d_c)$$
$$-c_R(f_i, \epsilon_\rho^*, c_{R,1}^*, c_{R,2}^*, d_c^*))^2, (28)$$

where $c_R(f, \epsilon_\rho, c_{R,1}, c_{R,2}, d_c)$ denotes the Rayleigh velocity for frequency f and parameters ($\epsilon_\rho, c_{R,1}, c_{R,2}, d_c$), and N is the number of frequencies taken into account in the calculation.
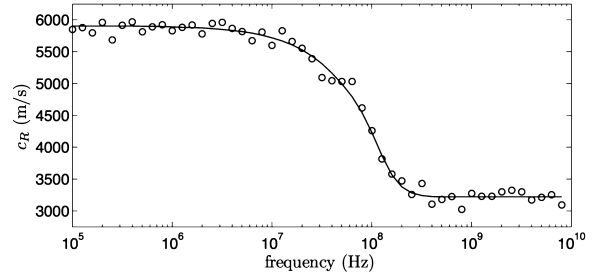
Fig. 10. Dispersion curve with (circles) and without added noise (full line) of the Rayleigh velocity for the fictive material defined in the text.

A possible problem complicating the reliable parameter retrieval is parametric degeneracy. In order to get some insight in possible pairwise degeneracy, the χ^2 cost function was evaluated around the best fitting values ($\epsilon_\rho^*, c_{R,1}^*, c_{R,2}^*, d_c^*$) for all parameter pairs. Fig. 11 shows the result by means of the contour plots for each of the six parameter pairs. If a genuine minimum in the χ^2 cost function exists in the contour plot for a particular parameter pair, then this infers that there is only one unique value of these parameters that minimizes the cost function. On the other hand, a valley of equivalent minima in a contour plot indicates interdependence between the two parameters of that particular pair.

In Fig. 11, the variation of each pair of parameters results in a genuine minimum, indicating a possible unique solution for the inverse problem of each pair of parameters. However, the steepness of the gradient in the cost function along each direction is different for different parameters. This indicates that the respective relative uncertainties vary. This behavior is inherent to Rayleigh waves. The correlation between two parameters with respect to the Rayleigh mode is witnessed by a long minimum valley. Zero correlation, i.e. parameters having a dissimilar influence on the Rayleigh mode, is reflected by a deep minimum, resulting in a steep gradient in all directions. E.g., while Fig. 11f shows that the Rayleigh velocities $c_{R,1}$ and $c_{R,2}$ are only weakly correlated, the rather long minimum valley in Fig. 11a indicates the existence of a relatively large correlation between coating thickness and density ratio. This means that they influence the Rayleigh dispersion in a comparable way, which is corroborated by Fig. 7.

Focusing only on the pairwise covariance between the material parameters to investigate the degeneracy does not necessary reveal all existing covariance, since the other parameters can introduce the chance of threefold or higher-order degeneracy between the unknown fitting parameters. Evidently, it is impossible to visualize multifold covariances in three or higher dimensions in a regular two-dimensional contour plot. However, possible multifold interdependence can be investigated by performing a so-called most-squares (MSQ) analysis [55,11], rather than a least-aquares (LSQ) analysis.

Although the real strength of the MSQ approach lies in the handling of multifold covariance, the MSQ principle is most easily explained for twofold correlation. Fig. 12 illustrates how a LSQ analysis underestimates the error on the parameter estimation, by means of an artificial example of a fit with 2 parameters. The LSQ approach finds parameter a by looking for the minimum of χ^2 as a function of a while keeping parameter b fixed to its global best fitting value, which equals zero in this case. This amounts to looking for the minimum of the red parabola in the bottom subfigure. The fitting uncertainty on parameter a is derived from the width of this red curve. The MSQ analysis, on the other hand, takes fitting covariance into account by considering, for every value of a, the local minimum value of χ^2 by using the optimum value of b. This is shown in the left subfigure and the resulting χ^2 is
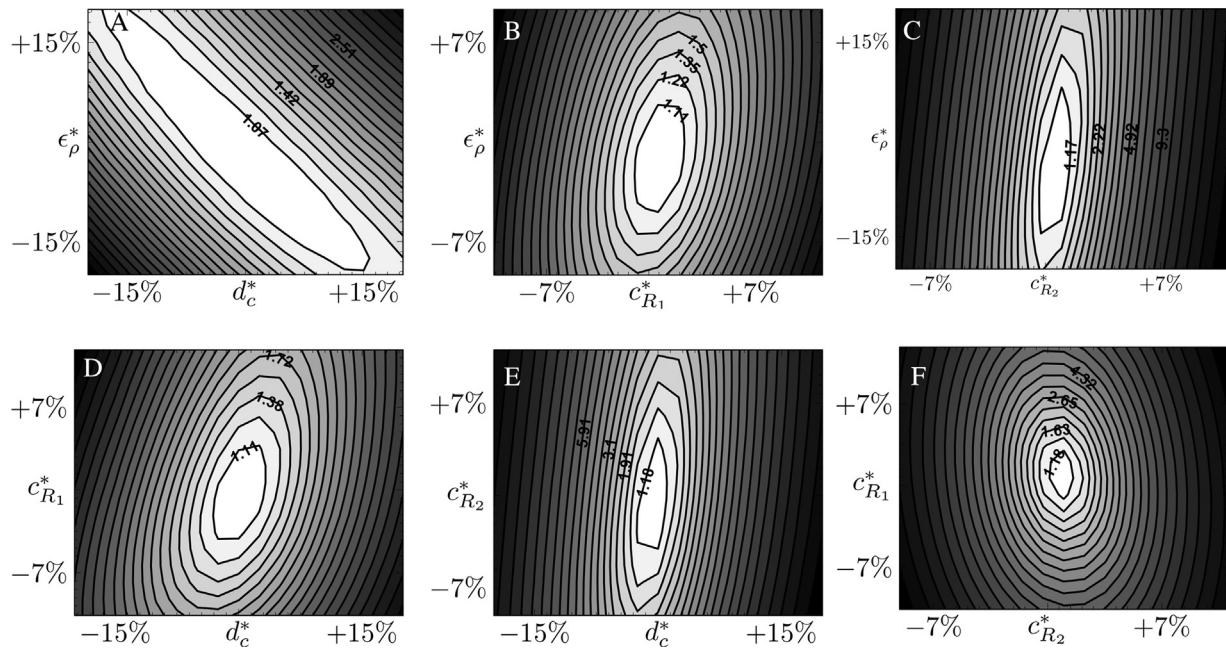
Fig. 11. Contour plots of the χ^2 cost function Eq. (28) using 50 frequencies, for the fictive material defined in the text. For some of the contour lines, the corresponding values of the cost function are indicated.
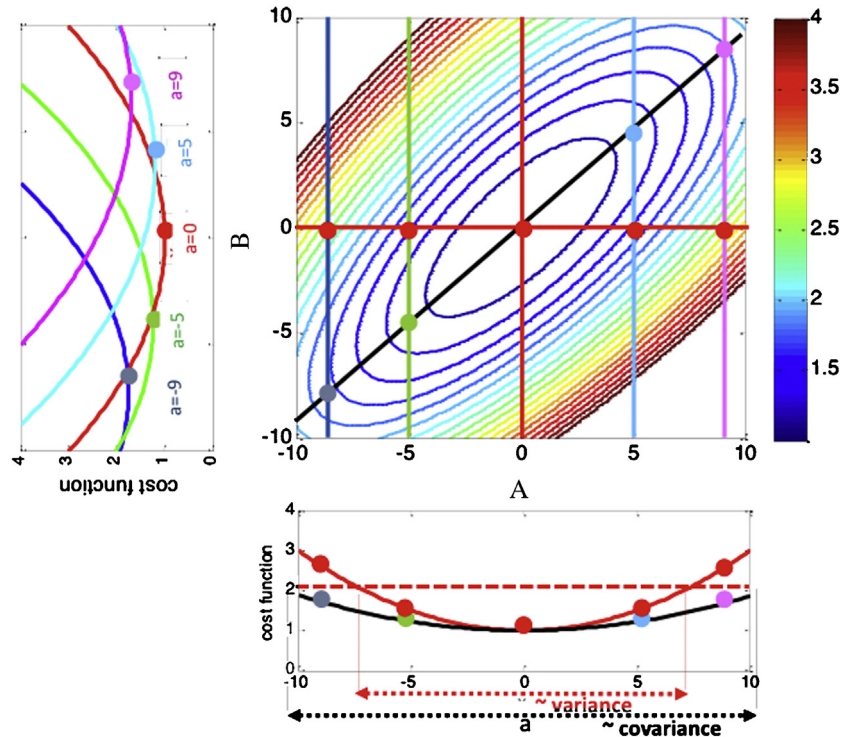
Fig. 12. Contour plot (top right) of cost function for a fitting problem with two fitting parameters a and b, each with best fitting value 0. Cost function as a function of a for global best fitting value $b = 0$ (bottom, red line) and for local best fitting value of b (bottom, black line). Cost function as a function of b (left) for various values of a, leading to the black line.

depicted as the black curve in the bottom subfigure. In this way, the colored dots monitor the variation of χ^2 along the stretched valley seen as the black diagonal line in the contour plot. Since the minima along this valley are lower than the values along the line $b = 0$, the corresponding width of the valley is larger. This means that the MSQ uncertainties on the fitting parameters, which are derived from the width of the stretched diagonal valley, are larger and more realistic than the respective LSQ errors. An extreme

situation would exist when a and b are interdependent. This occurs when different combinations of parameters a and b produce the same minimum value for χ^2, resulting in a minimum valley in parameter space and infinite width for the χ^2_{MSQ} parabola. Then the considered parameters cannot be determined independently, which leads to an ill-posed inverse problem [56]. While MSQ analysis reveals the problem, LSQ analysis does not. Finally, due to the more detailed parameter search around the best least squares
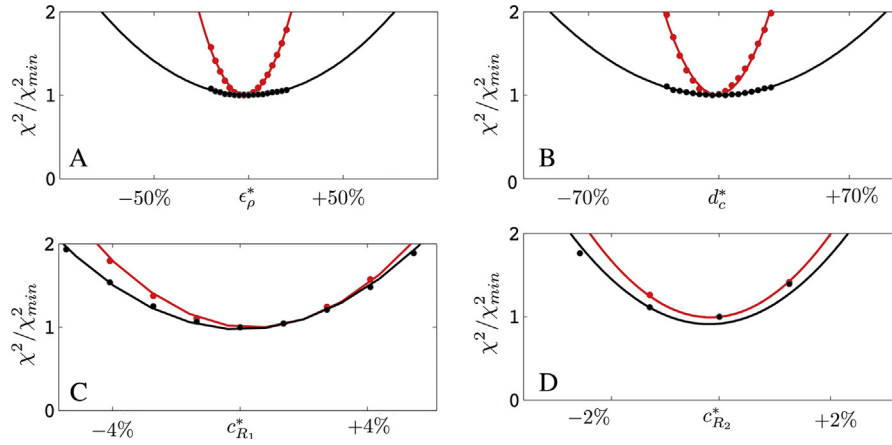
Fig. 13. Dependence of the LSQ (red) and MSQ (black) cost functions on the four fitting parameters for a simulated experimental Rayleigh dispersion together with their corresponding fitted parabolae.

minimum during the most squares scanning of the cost function, the position of the minimum found by the MSQ procedure in Fig. 13c is more reliable than the LSQ minimum. All this comes at a price, as the MSQ approach requires considerably more computing power than the LSQ fitting procedure, because the minimizations take place in a higher-dimensional parameter space.

Fig. 13 shows the dependence of χ^2_{MSQ} and χ^2_{LSQ} on each of the parameters considered in the present feasibility study. The fact that the most squares parabolae exhibit a distinct minimum indicates that there is no multifold fitting parameter degeneracy and that the inverse problem is well-posed. This indicates that in principle SAW laser ultrasonic spectroscopy allows to estimate four of the seven acoustic parameters required to obtain the elastic properties of the two layers.

As expected, the most squares minima are broader than the least squares minima, especially for the parameters ϵ_ρ and d_c. This means that the corresponding uncertainty on their retrieved values is greater than as suggested by an LSQ analysis. In general, the least squares fitting uncertainty $\sigma_{p,LSQ}$ of parameter p with real value p^* can be determined by [57]

$$\sigma_{p,LSQ} = \sqrt{\frac{2}{(N-P)\frac{\partial^2}{\partial p^2}\left(\frac{\chi^2_{LSQ}(p)}{\chi^2(p^*)}\right)}}, \tag{29}$$

where P is the number of fit parameters, which equals 4 for our parameter set ($\epsilon_\rho, c_{R_1}, c_{R_2}, d$). Due to the parabolic form of the cost function near its minimum, this is equivalent to

$$\sigma_{p,LSQ} = \frac{1}{\sqrt{N-P}} w_{LSQ}, \tag{30}$$

where w_{LSQ} is the width of the parabola ($\chi^2_{LSQ}(p)/\chi^2(p^*)$) at the level 2. As such, the fitting uncertainty of each parameter can be read out directly from Fig. 13. Analogously, the most squares fitting uncertainty of a parameter p can be written as

$$\sigma_{p,MSQ} = \frac{1}{\sqrt{N-P}} w_{MSQ}, \tag{31}$$

where w_{MSQ} is the width of the parabola ($\chi^2_{MSQ}(p)/\chi^2(p^*)$) at the level 2.

For the present example with the four parameters, Eq. (31) yields the MSQ uncertainties ($\Delta\epsilon_\rho/\epsilon_\rho = 75\%$, $\Delta d_c/d_c = 90\%$, $\Delta c_{R_1}/c_{R_1} = 5.5\%$, $\Delta c_{R_2}/c_{R_2} = 2.5\%$). At first sight, it may seem strange that the uncertainty on the retrieved coating thickness as predicted by the MSQ analysis turns out so big, while Fig. 7 shows a strong influence of the coating thickness on the transition frequency. But a closer look shows that this is due to the correlation

between d and ϵ_ρ, rendering both values much less certain. Remark that the LSQ values of the uncertainties ($\Delta\epsilon_\rho/\epsilon_\rho = 25\%$, $\Delta d_c/d_c = 30\%$) are three times smaller than the MSQ values. The LSQ approach fails to recognize the correlation and hence puts too much faith in the retrieved values.

In a similar way as for the acoustic dispersion curve, the inverse problem can also be solved for a thermal dispersion curve, aiming at the extraction of the thermal diffusivity of the two layers in a coating-substrate material. Both elastic and thermal material parameters enter this low-frequency signal, so that it can be expected that they have a mixed influence on the thermal dispersion curve. However, here we assume that the elastic properties of both materials are well-established, so that only the thermal diffusivities and the coating thickness ($\alpha_1^* = 2 \cdot 10^{-5}$ m²/s, $\alpha_2^* = 10^{-5}$ m²/s, $d_c^* = 10^{-4}$ m) enter as unknown fitting parameters. Again, a least and most squares analysis was performed along the three-dimensional parameter space (α_1, α_2, d_c), with a cost function analogous to Eq. (28). Normally distributed white noise with a signal-to-noise ratio equal to 10 was added to the theoretic thermal dispersion curve in order to mimic an experimental trace, as shown in Fig. 14. The χ^2 contour plots in Fig. 15 all show an absolute regional minimum close to the exact values, confirming the expected absence of pairwise fitting degeneracy. The thermal diffusivity of the coating and the substrate determine the short and long wavelength limit of the thermal dispersion curve, respectively, while the coating thickness determines the location of the transition on the wavelength axis. In Fig. 16 the least and most squares parabola are shown for the three parameters, showing a genuine minimum in both the least and most squares cost functions. Again, this demonstrates that the thermal diffusivities and coating thickness can unambiguously be extracted from a thermal dispersion curve provided that the elastic properties are
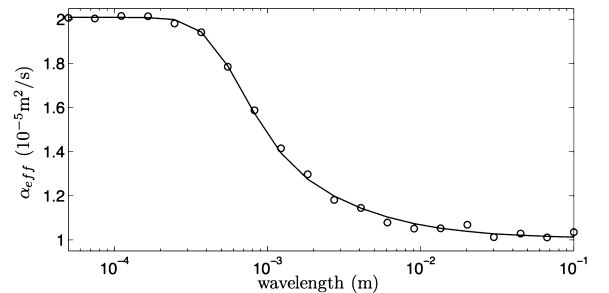
Fig. 14. Dispersion curve with (circles) and without added noise (full line) of the effective diffusivity for the fictive material defined in the text.
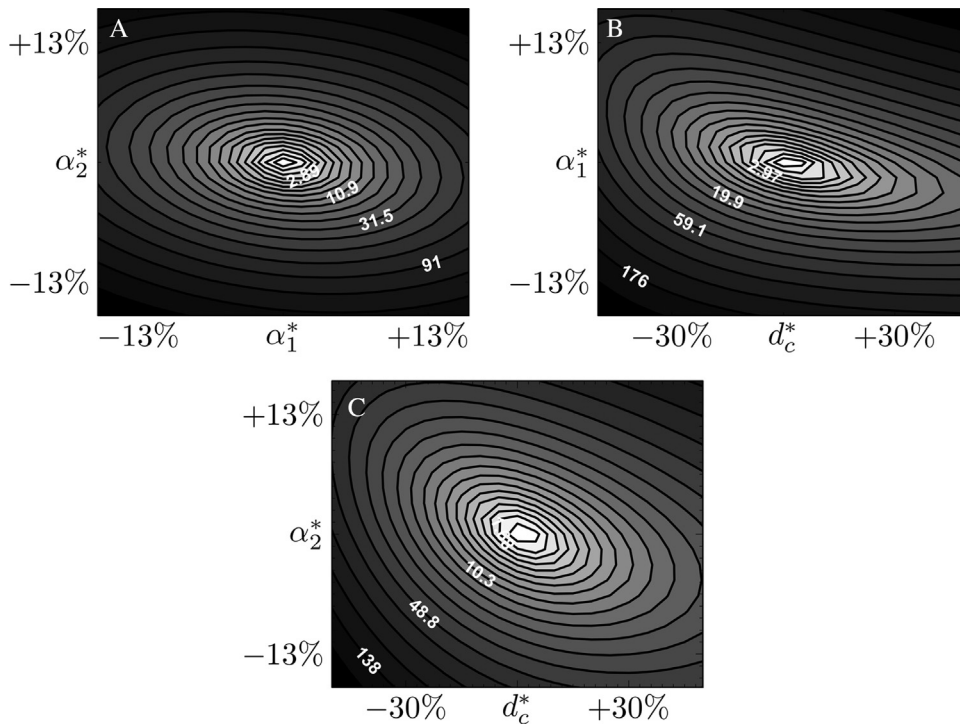
Fig. 15. Contour plots of the χ^2 cost function for the diffusivity, using 20 frequencies, for pairs of thermal coating-substrate parameters.
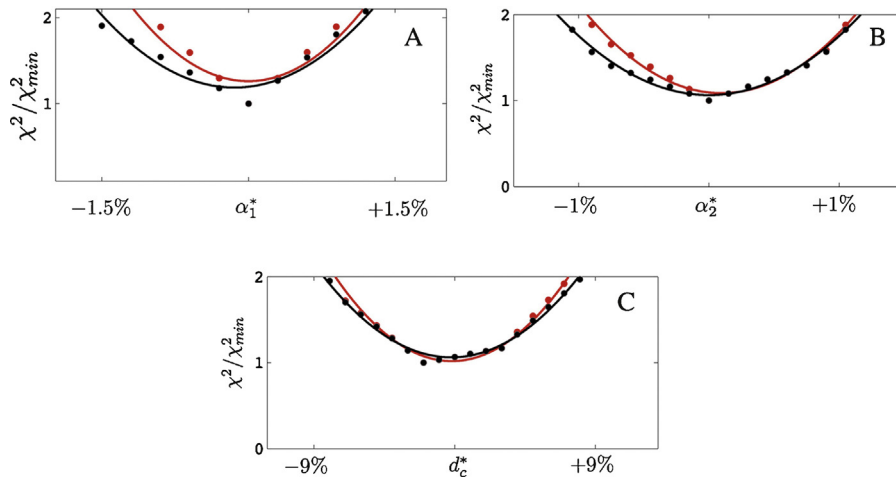

Fig. 16. Dependence of the least squares (red) and most squares (black) cost functions on the three thermal fitting parameters for a simulated experimental thermal dispersion curve, together with their corresponding fitted parabola.

known and that the dispersion curve is acquired over a sufficient broad wavelength range. The difference between the LSQ and MSQ uncertainties is now immaterial.

For completeness, it should be mentioned that in many experimental situations the uncertainty on measured quantities is mainly caused by systematic errors. The presented analysis of the effect of random errors should therefore be seen as giving information about the intrinsic and maximum attainable fitting quality, taking into account fitting covariance and degeneracy, for a finite number of measurement points affected by random noise.

5. Conclusions

The implementation of heterodyne detection of impulsive stimulated scattering signals was revisited, considering a differential measurement configuration in which both diffracted and specularly reflected probe beams are exploited. The underlying diffraction theory was elaborated for shallow ripple displacements. The modified detection scheme allows to remove dc signal contributions, the accompanying laser light fluctuation noise, and homodyne signal components from the signal. Expressions for the signal response allow to reliably predict the magnitude of transient grating ripples. Starting from expressions by Käding et al. for the decay of the photothermal part of ISS signals on semi-infinite substrates, the concept of thermal wave dispersion in coating-substrate configurations was introduced. This involves curves for the frequency or grating wavelength dependence of an effective diffusivity value that was determined by fitting the photothermal signal decay by a model for a homogeneous semi-infinite medium. The feasibility of

extracting relevant elastic and thermal characteristics from the photoacoustic and photothermal part of ISS signals was demonstrated on the basis of simulated data with typical levels of noise added. Taking into account the possible pairwise degeneracy of the acoustic parameters to express the elastic moduli of an isotropic material, it was shown by a least and most squares analysis that there exists no supplementary degeneracy in the fitting parameters for both the elastic and thermal dispersion curves. The analysis shows that both the acoustic and thermal inverse problems are well posed, and that ISS is a suitable technique to thermally and elastically characterize coating-substrate materials.

Conflict of interest statement

The authors declare that there are no conflicts of interest.

Acknowledgements

Appendix A. Thermoelastic response

We revisit the configuration of Fig. 2, assuming a homogeneous semi-infinite solid situated at negative y-values. If the heating produced by mechanical deformation is negligible, then the thermo-acoustic coupled equations for temperature $T(x, y, t)$ and displacement $\mathbf{u}(x, y, t)$ of the material can be approximated by [58]

$$\frac{1}{\alpha}\frac{\partial T}{\partial t} - \nabla^2 T = \frac{Q}{\kappa}, \tag{A.1}$$

$$\ddot{\mathbf{u}} - c_T^2 \nabla^2 \mathbf{u} - (c_L^2 - c_T^2)\nabla(\nabla \cdot \mathbf{u}) = -\gamma \nabla T, \tag{A.2}$$

where $Q(x, y, t)$ is the absorbed heat power density, κ the thermal conductivity, α the thermal diffusivity, c_L and c_T are the longitudinal and transverse bulk wave velocities, while the thermo-elastic coupling constant is given by $\gamma = (3c_L^2 - 4c_T^2)\alpha_{\text{th}}$, where α_{th} is the thermal expansion coefficient.

For ISS we can restrict $Q(x, y, t)$ to its spatially periodic part, which according to Eq. (3) is given by

$$Q(x, y, t) = I_{\text{pu}}(t)(1 - r)\beta e^{\beta y}\cos(Kx), \tag{A.3}$$

where r is the surface reflectivity and β the optical absorption coefficient for the optical wavelength of the laser light. The resulting temperature evolution can then be rewritten as

$$T(x, y, t) = \overline{T}(y, t)\cos(Kx), \tag{A.4}$$

and in frequency domain Eq.(A.1) turns into

$$\sigma^2(y, \omega) - \frac{\partial^2 \overline{T}(y, \omega)}{\partial^2 y} = \frac{(1 - r)I_{\text{pu}}(\omega)}{\kappa}\beta e^{\beta y}, \tag{A.5}$$

with $\sigma = \sqrt{K^2 + i\omega/\alpha}$. Assuming boundedness of temperature and zero heat loss to positive y-values ($\partial \overline{T}/\partial y|_{y=0} = 0$) the solution reads as

$$\overline{T}(y, \omega) = \frac{I_{\text{pu}}(\omega)(1 - r)\beta}{\kappa(\sigma^2 - \beta^2)}\left(-\frac{\beta}{\sigma}e^{\sigma y} + e^{\beta y}\right). \tag{A.6}$$

The temperature variations act as a driving force for the displacements, which are most conveniently found by using the Helmholtz decomposition [59]

$$\mathbf{u} = \nabla\varphi(x, y, t) + \nabla \times \boldsymbol{\psi}(x, y, t). \tag{A.7}$$

Using Eq. (A.7), Eq. (A.2) becomes

$$\nabla^2\varphi - \frac{1}{c_L^2}\ddot{\varphi} = \frac{\gamma}{c_L^2}T, \tag{A.8}$$

$$\nabla^2\boldsymbol{\psi} - \frac{1}{c_T^2}\ddot{\boldsymbol{\psi}} = 0, \tag{A.9}$$

where due to translation symmetry in the z-direction, $\boldsymbol{\psi} = (0, 0, \psi)$. In frequency domain, the solution for the potentials then reads

$$\varphi(x, y, \omega) = \left(\varphi_1 e^{p_L y} + \varphi_2 e^{\sigma y} + \varphi_3 e^{\beta y}\right)\cos(Kx), \tag{A.10}$$

$$\psi(x, y, \omega) = (i\psi_1 e^{p_T y})\sin(Kx), \tag{A.11}$$

with

$$\varphi_2 = -\frac{\gamma(1 - r)I_{\text{pu}}(\omega)\beta^2}{c_L^2\kappa\sigma(\sigma^2 - \beta^2)(\sigma^2 - p_L^2)}, \tag{A.12}$$

$$\varphi_3 = \frac{\gamma(1 - r)I_{\text{pu}}(\omega)\beta}{c_L^2\kappa(\sigma^2 - \beta^2)(\beta^2 - p_L^2)}, \tag{A.13}$$

$$p_{L,T} = \sqrt{K^2 - \omega^2/c_{L,T}^2}. \tag{A.14}$$

The integration constants φ_1 and ψ_1 can be found by introducing stress-free boundary conditions at the free surface $y = 0$ of the material, which read as [60]

$$\sigma_{xy}|_{y=0} = \rho c_T^2\left(\frac{\partial u_x}{\partial y} + \frac{\partial u_y}{\partial x}\right)\bigg|_{y=0} = 0, \tag{A.15}$$

$$\sigma_{yy}|_{y=0} = \rho\left((c_L^2 - 2c_T^2)\frac{\partial u_x}{\partial x} + c_L^2\frac{\partial u_y}{\partial y} - \gamma T\right)\bigg|_{y=0} = 0, \tag{A.16}$$

yielding

$$\begin{pmatrix}\varphi_1 \\ \psi_1\end{pmatrix} = \frac{1}{D_R}\begin{pmatrix}K^2 + p_T^2 & 2iK p_T \\ -2iK p_L & K^2 + p_T^2\end{pmatrix} \cdot S, \tag{A.17}$$

where D_R is the Rayleigh determinant given by

$$D_R = K^4 + 2K^2 p_T^2 + p_T^4 - 4K^2 p_T p_L, \tag{A.18}$$

and S is given by

$$S = \begin{pmatrix}K^2(\varphi_2 + \varphi_3)\left(\frac{c_L^2}{c_T^2} - 2\right) - \frac{c_L^2}{c_T^2}\left(\sigma^2\varphi_2 + \beta^2\varphi_3\right) + \frac{\gamma}{c_T^2}\overline{T}(y = 0, \omega) \\ -2iK(\sigma\varphi_2 + \beta\varphi_3)\end{pmatrix}. \tag{A.19}$$

Since the displacements are very small compared with $1/K$, the surface ripple due to the excited waves corresponds with $u_y(x, y = 0, t)$, which according to Eq. (A.7) is now given in time domain by

$$u_y(x, y = 0, t) = A(t)\cos(Kx), \tag{A.20}$$

in correspondence with Eq. (5), where the modulated amplitude $A(t)$ is given by

$$A(t) = \int_{-\infty}^{+\infty} e^{i\omega t}(p_L\varphi_1 + \sigma\varphi_2 + \beta\varphi_3 - iK\psi_1)d\omega. \tag{A.21}$$

References

[1] C. Glorieux, W. Gao, S. Kruger, K. Van de Rostyne, W. Lauriks, J. Thoen, Surface acoustic wave depth profiling of elastically inhomogeneous materials, J. Appl. Phys. 88 (7) (2000) 4394–4400.

[2] J. Meth, C. Marshall, M. Fayer, Experimental and theoretical analysis of transient grating generation and detection of acoustic waveguide modes in ultrathin solids, J. Appl. Phys. 67 (7) (1990) 3362–3377.

[3] E. Abramson, J. Brown, L. Slutsky, Applications of impulsive stimulated scattering in the earth and planetary sciences, Annu. Rev. Phys. Chem. 50 (1) (1999) 279–313.

[4] P. Korpiun, B. Merté, G. Fritsch, R. Tilgner, E. Lüscher, Photoacoustic method for the measurement of the thermal diffusivity of drawn foils, Colloid. Polym. Sci. 261 (4) (1983) 312–318.

[5] L. Williams, R. Anderson, M. Banet, Time-resolved ultrafast spectroscopy of coherent optical phonons and charge carriers in tetragonal mercuric iodide, Chem. Phys. Lett. 182 (5) (1991) 422–428.

[6] A. Mandelis, Photoacoustic and Thermal Wave Phenomena in Semiconductors, Elsevier Science Pub. Co., Inc., New York, NY, 1987.

[7] O. Zelaya-Angel, J. Alvarado-Gil, R. Lozada-Morales, H. Vargas, A. Ferreira da Silva, Band-gap shift in CdS semiconductor by photoacoustic spectroscopy: evidence of a cubic to hexagonal lattice transition, Appl. Phys. Lett. 64 (3) (1994) 291–293.

[8] W. Gao, V. Gusev, C. Glorieux, J. Thoen, G. Borghs, Supersonic radiative transport of electron-hole plasma in semiconductors at room temperature studied by laser ultrasonics, Opt. Commun. 143 (1) (1997) 19–24.

[9] C. Thomsen, H.T. Grahn, H.J. Maris, J. Tauc, Surface generation and detection of phonons by picosecond light pulses, Phys. Rev. B 34 (6) (1986) 4129.

[10] J. Rogers, K. Nelson, Study of lamb acoustic waveguide modes in unsupported polyimide thin films using real-time impulsive stimulated thermal scattering, J. Appl. Phys. 75 (3) (1994) 1534–1556.

[11] R. Salenbien, R. Côte, J. Goossens, P. Limaye, R. Labie, C. Glorieux, Laser-based surface acoustic wave dispersion spectroscopy for extraction of thicknesses, depth, and elastic parameters of a subsurface layer: feasibility study on intermetallic layer structure in integrated circuit solder joint, J. Appl. Phys. 109 (9) (2011) 093104.

[12] G. Andriamonje, V. Pouget, Y. Ousten, D. Lewis, Y. Danto, J.-M. Rampnoux, Y. Ezzahri, S. Dilhaire, S. Grauby, W. Claeys, et al., Application of picosecond ultrasonics to non-destructive analysis in VLSI circuits, Microelctron. Reliab. 43 (9–11) (2003) 1803–1807.

[13] H.-N. Lin, H. Maris, L. Freund, K. Lee, H. Luhn, D. Kern, Study of vibrational modes of gold nanostructures by picosecond ultrasonics, J. Appl. Phys. 73 (1) (1993) 37–45.

[14] A.M. Lomonosov, P.V. Grigoriev, P. Hess, Sizing of partially closed surface-breaking microcracks with broadband Rayleigh waves, J. Appl. Phys. 105 (8) (2009) 084906.

[15] O.B. Wright, K. Kawashima, Ultrasonic detection from picosecond surface vibrations: application to interfacial layer detection, Jpn. J. Appl. Phys. 32 (part 1) (1993) 2452–2454.

[16] W. Gao, C. Glorieux, J. Thoen, Laser ultrasonic study of lamb waves: determination of the thickness and velocities of a thin plate, Int. J. Eng. Sci. 41 (2) (2003) 219–228.

[17] Y. Sohn, S. Krishnaswamy, Interaction of a scanning laser-generated ultrasonic line source with a surface-breaking flaw, J. Acoust. Soc. Am. 115 (2004) 172.

[18] D. Schneider, M. Tucker, Non-destructive characterization and evaluation of thin films by laser-induced ultrasonic surface waves, Thin Solid Films 290 (1996) 305–311.

[19] J. Sermeus, R. Sinha, K. Vanstreels, P. Vereecken, C. Glorieux, Determination of elastic properties of a MnO$_2$ coating by surface acoustic wave velocity dispersion analysis, J. Appl. Phys. 116 (2) (2014) 023503 (7).

[20] R. Slayton, K. Nelson, A. Maznev, Transient grating measurements of film thickness in multilayer metal films, J. Appl. Phys. 90 (9) (2001) 4392–4402.

[21] J. Rogers, A. Maznev, M. Banet, K. Nelson, Optical generation and characterization of acoustic waves in thin films: fundamentals and applications, Annu. Rev. Mater. Sci. 30 (2000) 117–157.

[22] A. Maznev, A. Mazurenko, L. Zhuoyun, M. Gostein, Laser-based surface acoustic wave spectrometer for industrial applications, Rev. Sci. Instrum. 74 (1) (2003) 667–669.

[23] M. Fayer, Picosecond holographic grating generation of ultrasonic waves, IEEE J. Quantum Elect. 22 (8) (1986) 1437–1452.

[24] A. Harata, H. Nishimura, T. Sawada, Laser-induced surface acoustic waves and photothermal surface gratings generated by crossing two pulsed laser beams, Appl. Phys. Lett. 57 (2) (1990) 132–134.

[25] M.A. Buntine, D.W. Chandler, C.C. Hayden, Detection of vibrational-overtone excitation in water via laser-induced grating spectroscopy, J. Chem. Phys. 102 (1995) 2718.

[26] H. Eichler, Laser-induced grating phenomena, J. Mod. Optic. 24 (6) (1977) 631–642.

[27] Y. Yan, E. Gamble Jr., K. Nelson, Impulsive stimulated scattering: general importance in femtosecond laser pulse interactions with matter, and spectroscopic applications, J. Chem. Phys. 83 (1985) 5391.

[28] Y.-X. Yan, K.A. Nelson, Impulsive stimulated light scattering. I. General theory, J. Chem. Phys. 87 (1987) 6240.

[29] K.A. Nelson, R. Miller, D. Lutz, M. Fayer, Optical generation of tunable ultrasonic waves, J. Appl. Phys. 53 (2) (1982) 1144–1149.

[30] J. Monchalin, Optical detection of ultrasound, IEEE T. Ultrason. Ferr. 33 (1986) 485–499.

[31] H. Cho, H. Sato, H. Nishino, Y. Tsukahara, M. Inaba, A. Sato, M. Takemoto, S. Nakano, K. Yamanaka, Nondestructive evaluation of elastic properties in porous silicon film on Si(100) by the phase velocity scanning of laser interference fringes, Proceedings of the Ultrasonics Symposium, 1995 IEEE, vol. 1, 1995, pp. 757–760.

[32] J. Opsal, A. Rosencwaig, D. Willenborg, Thermal-wave detection and thin-film thickness measurements with laser beam deflection, Appl. Optics 22 (20) (1983) 3169–3176.

[33] A. Frass, P. Hess, Excitation of elastic surface pulses by fiber optics and near-field optical devices, J. Appl. Phys. 90 (10) (2001) 5090–5096.

[34] J. Monchalin, et al., Broadband optical detection of ultrasound by two-wave mixing in a photorefractive crystal, Appl. Phys. Lett. 59 (25) (1991) 3233–3235.

[35] J.-P. Monchalin, Optical detection of ultrasound at a distance using a confocal Fabry–Perot interferometer, Appl. Phys. Lett. 47 (1) (1985) 14–16.

[36] A. Maznev, K. Nelson, J. Rogers, Optical heterodyne detection of laser-induced gratings, Opt. Lett. 23 (16) (1998) 1319–1321.

[37] M. Clark, Optical detection of ultrasound on rough surfaces using speckle correlated spatial filtering, J. Phys. C: Conf. Ser. 278 (2011) 012025.

[38] R.J. Dewhurst, Q. Shan, Optical remote measurement of ultrasound, Meas. Sci. Technol. 10 (1999) R139–R168.

[39] C.B. Scruby, L.E. Drain, Laser Ultrasonics Techniques and Applications, Taylor & Francis, 1990.

[40] J. Xiong, C. Glorieux, Spectrally resolved detection of mixed acoustic vibrations by photorefractive interferometry, J. Appl. Phys. 113 (5) (2013) 054502.

[41] I. Arias, J. Achenbach, Thermoelastic generation of ultrasound by line-focused laser irradiation, Int. J. Solids Struct. 40 (25) (2003) 6917–6935.

[42] E. Popov, L. Tsonev, E. Loewen, Scalar theory of transmission relief gratings, Opt. Commun. 80 (5) (1991) 307–311.

[43] D. Haojiang, G. Fenglin, H. Pengfei, General solutions of coupled thermoelastic problem, Appl. Math. Mech. 21 (6) (2000) 631–636.

[44] J. Wauer, T. Rother, Considerations to Rayleigh's hypothesis, Opt. Commun. 282 (3) (2009) 339–350.

[45] V. Gusev, C. Desmet, W. Lauriks, C. Glorieux, J. Thoen, Theory of Scholte, leaky Rayleigh, and lateral wave excitation via the laser-induced thermoelastic effect, J. Acoust. Soc. Am. 100 (1996) 1514.

[46] L.V. Ahlfors, Complex Analysis: An Introduction to the Theory of Analytic Functions of One Complex Variable, International Series in Pure and Applied Mathematics, McGraw-Hill, New York, 1979.

[47] I.A. Viktorov, Rayleigh and Lamb Waves: Physical Theory and Applications, vol. 147, Plenum Press, New York, 1967.

[48] J. Sermeus, O. Matsuda, R. Salenbien, B. Verstraeten, J. Fivez, C. Glorieux, Thermoelastic model for impulsive stimulated scattering monitoring the evolution from capillary to Rayleigh type wave propagation on the surface of viscoelastic materials throughout the glass transition, Int. J. Thermophys. 33 (10–11) (2012) 2145–2158.

[49] C. Glorieux, K. Van de Rostyne, K. Nelson, W. Gao, W. Lauriks, J. Thoen, On the character of acoustic waves at the interface between hard and soft solids and liquids, J. Acoust. Soc. Am. 110 (2001) 1299.

[50] O. Käding, H. Skurk, A. Maznev, E. Matthias, Transient thermal gratings at surfaces for thermal characterization of bulk materials and thin films, Appl. Phys. A 61 (3) (1995) 253–261.

[51] L. Malacarne, N. Astrath, G. Lukasievicz, E. Lenzi, M. Baesso, S. Bialkowski, Time-resolved thermal lens and thermal mirror spectroscopy with sample-fluid heat coupling: a complete model for material characterization, Appl. Spectrosc. 65 (1) (2011) 99–104.

[52] D.M. Todorovic, B. Cretin, P. Vairac, Y.Q. Song, M.D. Rabasovic, D.D. Markushev, Laser-excited electronic and thermal elastic vibrations in a semiconductor rectangular plate, Int. J. Thermophys. 34 (8–9) (2013) 1712–1720.

[53] D.M. Todorovic, M.D. Rabasovic, D.D. Markushev, Photoacoustic elastic bending in thin film-substrate system, J. Appl. Phys. 114 (21) (2014).

[54] Z. Hadjoub, I. Beldi, M. Bouloudnine, A. Gacem, A. Doghmane, Thin film loading effects on SAW velocity dispersion curves, Electron. Lett. 34 (3) (1998) 313–315.

[55] D.D. Jackson, Most squares inversion, J. Geophys. Res. 81 (5) (1976) 1027–1030.

[56] P.C. Menon, R.N. Rajesh, C. Glorieux, High accuracy, self-calibrating photopyroelectric device for the absolute determination of thermal conductivity and thermal effusivity of liquids, Rev. Sci. Instrum. 80 (5) (2009) 054904.

[57] P.R. Bevington, Data Reduction and Error Analysis for the Physical Sciences, McGraw-Hill, New York, 1969.

[58] A. Rosencwaig, A. Gersho, Theory of the photoacoustic effect with solids, J. Appl. Phys. 47 (1) (1976) 64–69.

[59] H. Schey, Div, Grad, Curl, and All That, W.W. Norton Company, New York, 1996.

[60] A. Duggal, J. Rogers, K. Nelson, Real-time optical characterization of surface acoustic modes of polyimide thin-film coatings, J. Appl. Phys. 72 (7) (1992) 2823–2839.

Bert Verstraeten, born April 15, 1986 in Bree, Belgium. He obtained his Master's degree in Physics at the KU Leuven in 2009, after which he started a PhD on the topic "Development of a diagnostic method for thermoelastic characterization of coatings using laser ultrasonics" at the Laboratory of Acoustics and Thermal Physics, connected to the Physics and Astronomy Department of KU Leuven. This PhD work was funded by a research scholarship granted by SCK-CEN and F.W.O. He successfully defended his PhD project in September 2013. At this moment, Bert Verstraeten works for ASML in the Netherlands.

Jan Sermeus born august 2nd 1986 in Leuven, obtained his Master in physics of soft matter at the KU Leuven in 2010. During his Master thesis he worked on ISTS based excitation and detection of capillary waves on free liquid surfaces, allowing the extraction of the surface tension. In his PhD work the technique remained the same, however the focus shifted towards thin films on anisotropic substrates. He, successfully, defended his PhD in the summer of 2014. Both his Master thesis and PhD thesis were done at the Laboratory of Acoustics and Thermal Physics (ATF) at the KU Leuven under the supervision of Prof. Dr. Christ Glorieux. He is currently a scientific researcher at ATF.

Robbe Salenbien obtained his M.Sc. (cum laude) and PhD. in Physics at the KU Leuven, in 2007 and 2012, respectively. He was involved in photoacoustic and photothermalstudies of ultrathin structures and visco-elastic materials. In 2012, he joined the Flemish Institute for technological research (VITO) as a researcher in energy technology, focussing on smart district applications such as optimal thermal technology integration. He is engaged in different national and international relevant research projects, e.g. FP7 Resilient, IWT-VIS Smart Geotherm.

Jan Fivez started his career as a research assistant at the Universität des Saarlandes in Saarbrücken, Germany, and the University of Antwerp, Belgium, where he obtained his PhD in 1982 with a study of the interaction of magnetic and acoustic behaviour of the solid state. After visiting the Acoustics and Thermal Physics group at the KU Leuven, he became interested in photo-acoustics and photothermal techniques, and this was the start of a long-term cooperation. He is particularly interested in the mathematical foundation of inverse techniques for the non-destructive evaluation of thermal and mechanical properties of solids.

Gennady Shkerdin, born March 26, 1946, in Pensa region, USSR, graduated in physics at Moscow Institute of Physics and Technology in 1971 and obtained the Degree of Doctor of Sciences in physics and mathematics on the topic "Resonant and nonlinear acousto-optic interaction in solids" at the Institute of Radio Engineering and Electronics of Russian Academy of Sciences (IRE RAS) in 1983. Currently he is a leading scientist at IRE RAS. His research activities concern the studies of resonant photoelasticity in QW structures, acoustical waves interaction with imperfections in layered structures and the studies of fast optical phenomena for mid-IR applications.

Christ Glorieux born July 12, 1965, in Kuurne, Belgium, graduated in physics at the KU Leuven, Belgium in 1987 and obtained his Ph.D. degree in 1994 on the topic "Depth profiling of inhomogeneous materials and study of the critical behavior of gadolinium by photoacoustic and related techniques" at the Physics and Astronomy Department of K.U. Leuven. His research activities concern the determination of thermo-elastic properties of soft condensed matter, mainly by photoacoustic and photothermal techniques, with applications in thin film characterization and non-destructive testing. He is also leading a research division on Acoustics and Thermal Physics, and is involved in projects on the development of a bionic eye lens and high resolution adiabatic scanning calorimetry.